

# Accurate Simulation of RF MEMS VCO Performance Including Phase Noise

Manas Behera, Volodymyr Kratyuk, Sudipto K. De, Narayan R. Aluru, *Member, IEEE*, Yutao Hu, and Kartikeya Mayaram, *Fellow, IEEE*

**Abstract**—A new coupled circuit and electrostatic/mechanical simulator (COSMO) is presented for the design of low phase noise radio frequency (RF) microelectromechanical systems (MEMS) voltage-controlled oscillators (VCOs). The numerical solution of device level equations is used to accurately compute the capacitance of a MEMS capacitor. This coupled with a circuit simulator facilitates the simulation of circuits incorporating MEMS capacitors. In addition, the noise from the MEMS capacitor is combined with a nonlinear circuit-level noise analysis to determine the phase noise of RF MEMS VCO. Simulations of two different MEMS VCO architectures show good agreement with experimentally observed behavior. [1230]

**Index Terms**—Circuit simulation, coupled circuit and device simulation, electrostatic/mechanical simulator, microelectromechanical systems (MEMS) capacitor, microelectromechanical systems voltage-controlled oscillator (MEMS VCO), noise simulation, phase noise, radio frequency voltage-controlled oscillator (RF VCO).

## I. INTRODUCTION

SEVERAL computer-aided design tools for analysis and design of microelectromechanical devices have been developed to date based on various methodologies [1], [2]. For example, MEMCAD [3] uses ABAQUS, a commercial finite-element method (FEM) package for the mechanical analysis and a boundary-element method (BEM)-based program FASTCAP [4] for the electrostatic analysis. SOLIDIS [5] is an FEM-based tool tailored for coupled 3-D analysis of microactuators. Surface electrostatic forces, thermomechanics, and piezoelectric effects have been incorporated for the static analysis and optimization of MEMS actuators. CAEMEMS [6] is another FEM-based tool which has a process modeler that can model MEMS-relevant process sequences; and a device modeler that can perform finite-element simulations, link individual devices together through appropriate matrix operations, and perform simulations of entire mechanical systems. Newton-based methods for strong electromechanical coupling have been developed in [7], [8]. Efficient algorithms

Manuscript received December 18, 2003; revised July 16, 2004. This work is supported in part by NSF Grants CCR-0121616 and CCR-0120275, and by the SRC under Contract 2001-TJ-922. Subject Editor H. Zappe.

M. Behera and Y. Hu were with the School of Electrical Engineering and Computer Science, Oregon State University, Corvallis, OR 97331 USA. They are presently with Agilent Technologies, Santa Rosa, CA 95403 USA.

V. Kratyuk, and K. Mayaram are with the School of Electrical Engineering and Computer Science, Oregon State University, Corvallis, OR 97331 USA.

S. K. De and N. R. Aluru are with the Beckman Institute for Advanced Science and Technology, University of Illinois at Urbana-Champaign, Urbana, IL 61801 USA.

Digital Object Identifier 10.1109/JMEMS.2004.839317

for coupled electrostatic and mechanical analysis for statics [9] and dynamics [10] have been developed using Lagrangian electrostatics [11]. These device level tools can be coupled with a circuit simulator for the study of micro-electro-mechanical systems (MEMS). A coupled circuit and device simulator can facilitate accurate simulations of these systems even in the absence of proper macromodels for the MEMS devices. The behavior of different device structures can also be analyzed without having to construct a macromodel for each structure.

Recently, different configurations of the MEMS-based capacitor have been examined for improved tuning range [12], [13]. In addition to having a high Q factor and a wide tuning range, MEMS variable capacitors can also withstand large voltage swings, thus making them suitable for low phase noise voltage-controlled oscillator (VCO) applications [14], [15]. However, the absence of an accurate model for the MEMS variable capacitor has made it difficult to simulate the behavior of MEMS VCOs. This results in an extremely long design cycle or conservative design practices.

As a possible solution to these problems, a coupled circuit and device simulator for the improved design of MEMS-capacitor-based RF VCOs, COSMO, is presented in this paper. Coupled simulations can efficiently simulate the tuning characteristics and phase noise in RF MEMS VCOs. Comparisons between simulated results and existing experimental data demonstrate the accuracy of this approach.

The paper is organized as follows. A brief description of the circuit and device simulators and their integration in COSMO is presented in Section II. Three different MEMS capacitor structures and their design parameters are described in Section III. In Section IV, the simulated tuning characteristics of a 2.4-GHz inductance-capacitance (*LC*) cross-coupled MEMS VCO are presented. The effects of different MEMS capacitor structures and materials on the tuning characteristics of the VCO are illustrated and comparisons with experimentally observed behavior are presented. In Section V, the additional noise from MEMS-based capacitors that contributes to the total phase noise in RF MEMS VCOs is discussed followed by a detailed description of the phase noise simulation technique used in this work. Simulated phase noise results of an 800 MHz single-ended Colpitts MEMS VCO are illustrated in Section VI and comparisons between simulated results and existing measured data are presented. This is followed by conclusions in Section VII.

## II. COUPLED SIMULATOR FOR MEMS OSCILLATOR (COSMO)

In this section, we provide a brief description of the circuit simulator (SPICE3f5) and the device simulator (EM8.9) used in

our work. This is followed by a description of the capacitance computation and integration of these simulators for simulation of circuits incorporating MEMS capacitors.

#### A. The Circuit Simulator: SPICE3f5

All the components in an electrical circuit (resistors, capacitors, inductors, transistors, diodes, and independent sources) are described by their branch constitutive relations. These relations when associated with Kirchoff's conservation laws, form nonlinear differential algebraic equations. The most commonly used analysis in the design of VCO's is the time-domain transient analysis. In this analysis, time discretization is performed using an integration method, linearization is done by a Newton-Raphson method, and the algebraic system is solved using sparse matrix techniques. For each time step, the node voltages are computed, time-integration is applied to capacitors and inductors, and the Jacobian matrix for Newton's method is updated and solved for new values of node voltages. Newton iterations are performed until convergence. In addition, the local truncation error due to the time discretization is checked to determine if the time step is acceptable in terms of accuracy. If this error is too large, the time step is reduced and the computation is repeated. The details can be found in [16].

#### B. The Device Simulator: EM8.9 [9], [10]

EM8.9 is a simulator for electrostatic MEMS analysis using a meshless method. It employs the finite cloud method (FCM) for mechanical analysis and the boundary cloud method (BCM) for electrostatic analysis. FCM and BCM methods obviate the need for complicated and time consuming mesh generation. Lagrangian descriptions are used to map the electrostatic analysis to the undeformed geometry of conductors, thus eliminating the need for geometry updates and re-computation of the interpolation functions. The procedure for the self-consistent analysis of coupled electromechanical devices can be summarized as follows. Electrostatic analysis using BCM is done first to compute the surface charge density and the electrostatic pressure, which is then used in the mechanical analysis (performed on the undeformed geometry by FCM) to compute the structural displacement. This procedure is repeated until a state of equilibrium is achieved. Additional details on the algorithms can be found in [9], [10].

#### C. Capacitance Computation

As described above, EM8.9 solves for the structural displacement of the MEMS capacitors for a given applied voltage. The solution obtained from EM8.9 is used to compute the capacitance of the MEMS capacitor. The input to EM8.9 is specified in the form of the applied voltage, dimensions, geometry, number of discrete nodes and the material properties. A set of these input parameters defines a unique problem which is processed by EM8.9 in three phases.

The first phase is the *initialize* phase which involves reading in the input, discretization, generating nodes and memory allocation. The second phase is the *solve* phase where the structural displacement of each discrete element is computed along both

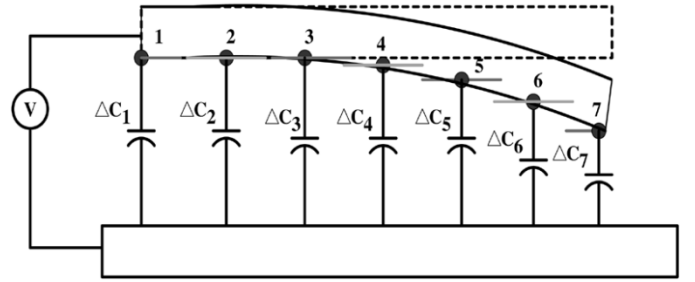


Fig. 1. Capacitance computation for the MEMS capacitor.

the x-axis and the y-axis and stored in the two-dimensional displacement vectors  $xdisp$  and  $ydisp$ . Finally, in the *update* phase the geometry and displacement vectors are updated. The *solve* and *update* phases are repeated until convergence is reached.

The capacitance is computed after the *solve* phase upon convergence. Since the displacement along the x-axis is small and assuming a sufficiently large number of nodes, each discrete element can be treated as a parallel-plate capacitor (Fig. 1) and the incremental capacitance between each element and the bottom plate can be computed. Finally, the total capacitance of the MEMS capacitor can be computed by adding all the incremental capacitances and is given by

$$C_{MEMS} = \frac{\epsilon_0 A}{2(N-1)} \left( \frac{1}{d_1} + 2 \sum_{j=2}^{N-1} \frac{1}{d_j} + \frac{1}{d_N} \right) \quad (1)$$

$$d_j = g_0 - ydisp(1, j) \quad (2)$$

where

$\epsilon_0 =$	permittivity of air;
$A =$	area of the top plate;
$N =$	number of discrete nodes along the length of the top plate;
$g_0 =$	gap between the two plates at zero applied voltage;
$ydisp(i, j) =$	vertical displacement of the $j$ th node along the length of the $i$ th surface of the top plate;
$(i = 1$	corresponds to the bottom surface.)

#### D. Software Integration

The circuit simulator SPICE3f5 and the electrostatic/mechanical simulator EM8.9 were integrated by using file processing and system calls. A block diagram illustrating the coupling between the two simulators is shown in Fig. 2. SPICE3 calls EM8.9 at every Newton iteration and passes the terminal voltages of the MEMS capacitor. EM8.9 computes and returns the capacitances and the circuit matrix is updated.

When the applied voltage exceeds the *pull-in* voltage, the device is unstable and hence the simulator does not converge. Therefore, a suitable voltage limiting scheme is used to avoid unnecessary device calls and, hence, reduce the computational cost.

### III. MEMS-BASED VARIABLE CAPACITORS

In this section, we describe the different MEMS capacitor structures that have been simulated using COSMO. These MEMS capacitors are manifestations of the same functional

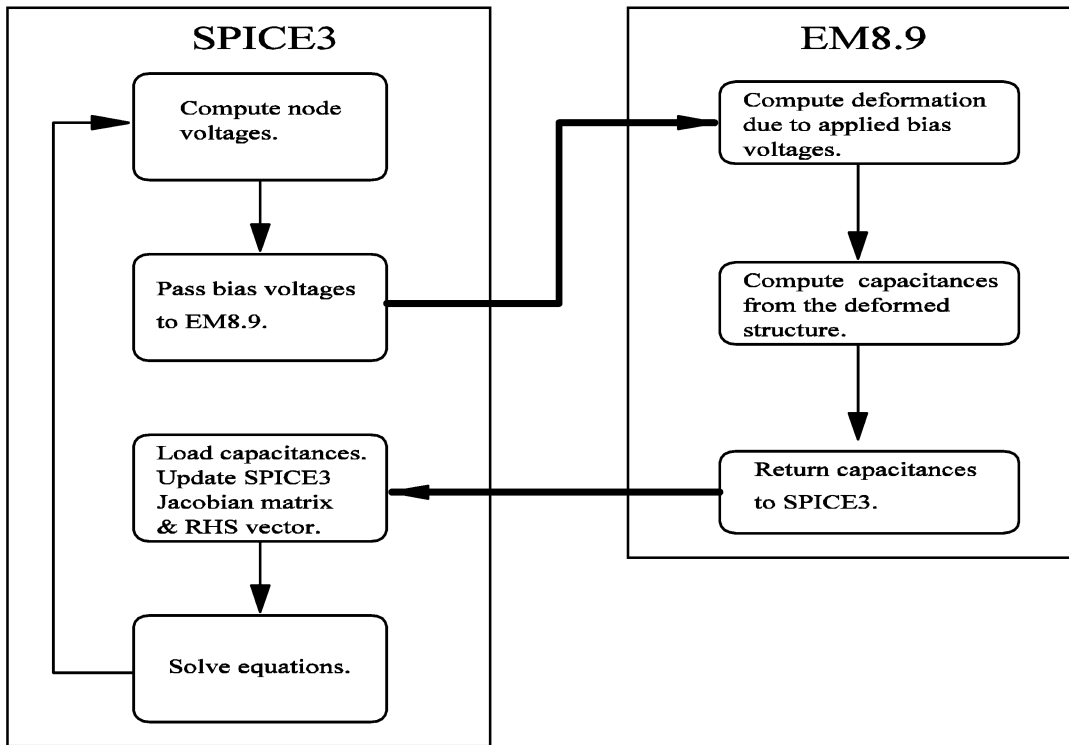


Fig. 2. The COSMO simulator showing coupling between SPICE3 and EM8.9.

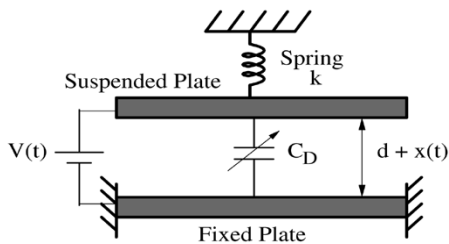


Fig. 3. Functional model of an electro-mechanically tunable parallel-plate capacitor.

model as shown in Fig. 3, [12], [13]. However, their structural differences result in varied tuning characteristics. The tuning characteristics will be illustrated in the next section.

#### A. Cantilever Beams and Fixed-Fixed Beams

Cantilever beams and fixed-fixed beams are the simplest forms of electrostatically actuated MEMS-based capacitor structures. These structures and their deformation due to the application of an applied voltage are shown in Fig. 4. Cantilever and fixed-fixed MEM devices have several potential applications in the area of RF systems [17]: switches, tunable capacitors, inductors, and filters. High frequency, IC compatible microelectromechanical IF filters have been developed in [18] based on coupled fixed-fixed beams. These beams have also been used in the development of band pass filters with tunable frequency and bandwidth [19]. Low loss frequency translation (mixing) and highly selective filtering of applied electrical signals has been demonstrated using these beams [20]. In this work, the performance of these structures as frequency tuning elements in RF VCO's is investigated.

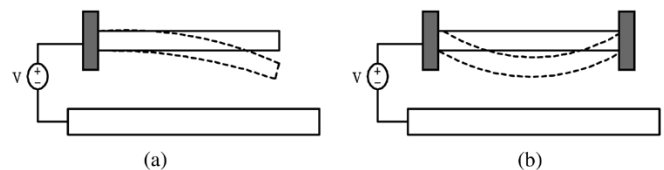


Fig. 4. Deformation due to an applied voltage for (a) cantilever beam and (b) fixed-fixed beam capacitor.

#### B. Two-Parallel-Plate Capacitor With Suspension Structures

Fig. 5 shows the top view of a two-parallel-plate MEMS-based capacitor with suspension structures [12], [15]. The suspension structures are designed to obtain the required stiffness constant and thus the desired tuning range [12]. These structures also introduce the top plate parasitic capacitance  $C_{TP}$  which can reduce the tuning range and lower the Q of the overall capacitor [21]. Furthermore, the suspension structures are also the dominant contributors of series resistance [12] which determines the Q of the device.

#### C. A Wide Tuning Range Three-Parallel-Plate Capacitor

A three-plate MEMS-based variable capacitor consisting of a suspended plate and two fixed plates is shown in Fig. 6. Since two dc voltages  $V_1$  and  $V_2$  can be used to either increase or decrease the desired capacitance  $C_D$ , a wider tuning range can be achieved [12]. It has been shown that the maximum theoretical tuning ratio of this three-parallel-plate MEMS-based capacitor is 2:1 [12]. However, the variable parasitic capacitance  $C_P$  limits the frequency tuning range of the VCO.

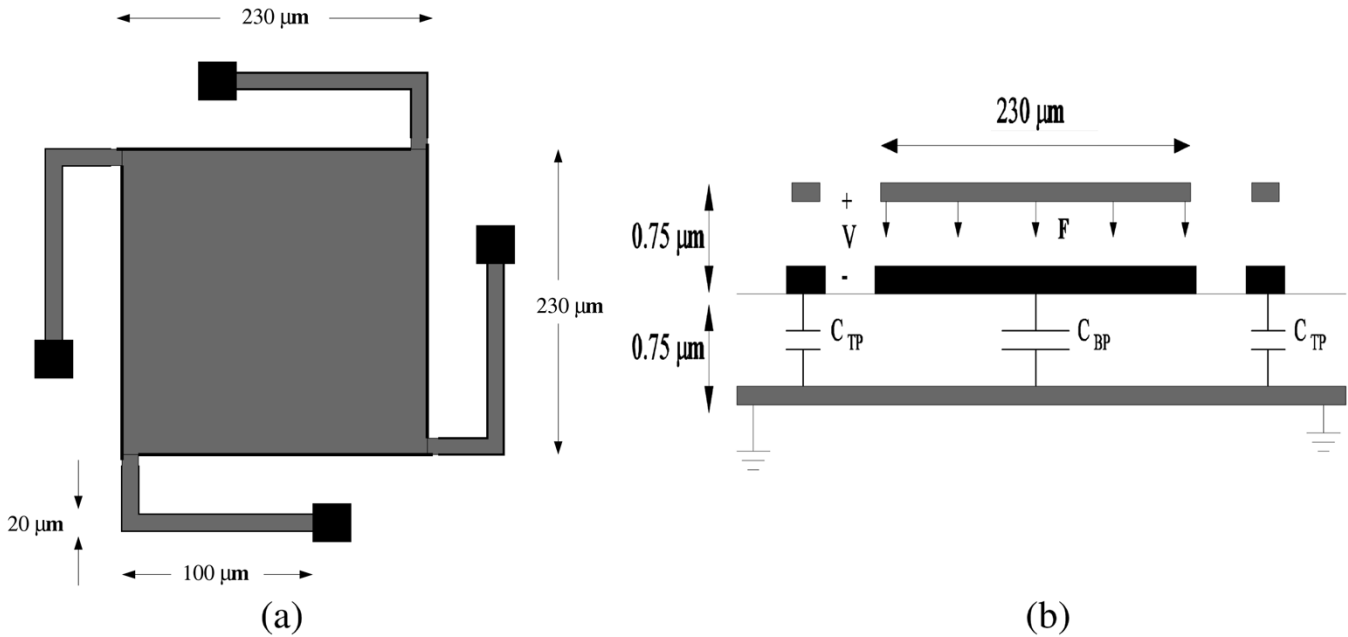


Fig. 5. (a) Top view and (b) cross-sectional view of the two-parallel-plate capacitor.

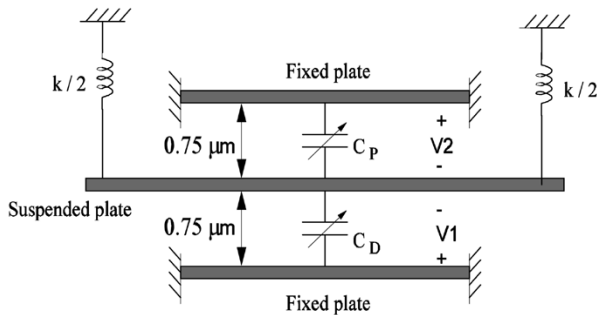


Fig. 6. Wide tuning range three-parallel-plate capacitor.

#### D. Lumped Element Models for the Devices

An efficient method of simulating a system consisting of different physical domains is by the use of lumped element equivalent circuits. In the case of MEMS-based capacitors, the displacement of the top plate in the mechanical domain can be represented by an equivalent capacitance in the electrical domain. One of the advantages of coupled circuit and device simulators is that they can readily simulate these lumped element equivalent circuits and are, therefore, highly accurate and reliable. In this work, the actual MEMS capacitor is simulated by EM8.9 and has been shown as a numerical device model in Fig. 7. The parasitics associated with the device have been represented by their equivalent circuit models as shown in Fig. 7. This combination of the numerical device model and the circuit models is simulated using COSMO.

The two-parallel-plate MEMS-based capacitors are modeled as two-terminal devices as shown in Fig. 7(a). The top plate parasitic capacitance  $C_{TP}$ , the series resistance  $R_S$  due to the suspension structure (shown as its parallel equivalent  $R_P$ ) and the bottom plate parasitic capacitance  $C_{BP}$  are independent of the applied voltage and, therefore, their values were easily calculated and included in the circuit. Since the cantilever and

fixed-fixed beams do not have suspension structures, the parasitic capacitance and series resistance were not included in their lumped models. The wide tuning range, three-parallel-plate MEMS-based capacitor was modeled as a three terminal device as shown in Fig. 7(b). Since the parasitic capacitance  $C_P$  is a function of the applied voltage  $V_2$ , it is included in the model along with the capacitance  $C_D$ . The calculated top plate parasitic capacitance and the series resistance due to the suspension structures were added in parallel to the MEMS capacitor.

#### IV. SIMULATED TUNING CHARACTERISTICS

A 2.4-GHz  $LC$  cross-coupled VCO [20] implemented in a HP 0.5- $\mu\text{m}$  CMOS technology was simulated to verify the tuning characteristics. The schematic of the VCO circuit is shown in Fig. 8(a). Fig. 8(b) shows the transient output of the VCO employing the two-parallel-plate capacitor. The different MEMS capacitor structures as described in Section III were employed for frequency tuning. An overlap area of  $230\ \mu\text{m} \times 230\ \mu\text{m}$  and an air gap of  $0.75\ \mu\text{m}$  were used for all the structures which results in a nominal capacitance of  $0.624\ \text{pF}$ . In order to maintain consistency with experimental results, pad parasitic capacitances of  $750\ \text{fF}$  were added in parallel to the MEMS capacitor. The suspension structures were designed to obtain a capacitance tuning ratio of 1.5:1 with a tuning voltage of 3.3 V. The length and width of the suspension structure were chosen as 100 and  $20\ \mu\text{m}$ , respectively.

The two-parallel-plate capacitor was simulated for different thicknesses of the top plate. The magnified version of the capacitance tuning characteristics for three different thicknesses is shown in Fig. 9. Since the top plate is nonrigid, it contributes to the overall stiffness constant of the MEMS capacitor. Hence, varying the thickness of the top plate alters the overall stiffness constant and therefore the tuning characteristics change.

The two-parallel-plate capacitor was also simulated for three different structural materials, polysilicon/gold, aluminum, and

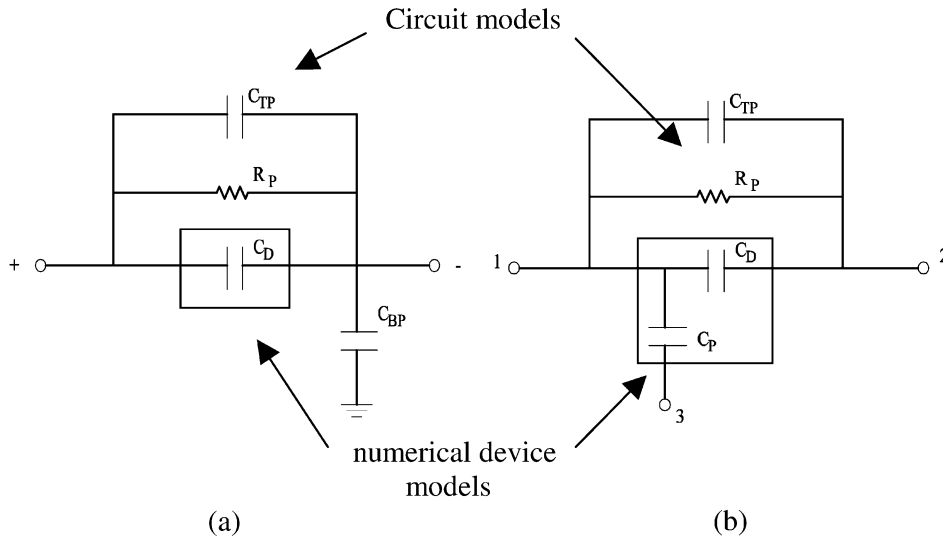


Fig. 7. Lumped model of (a) two-parallel-plate and (b) three-parallel-plate capacitor.

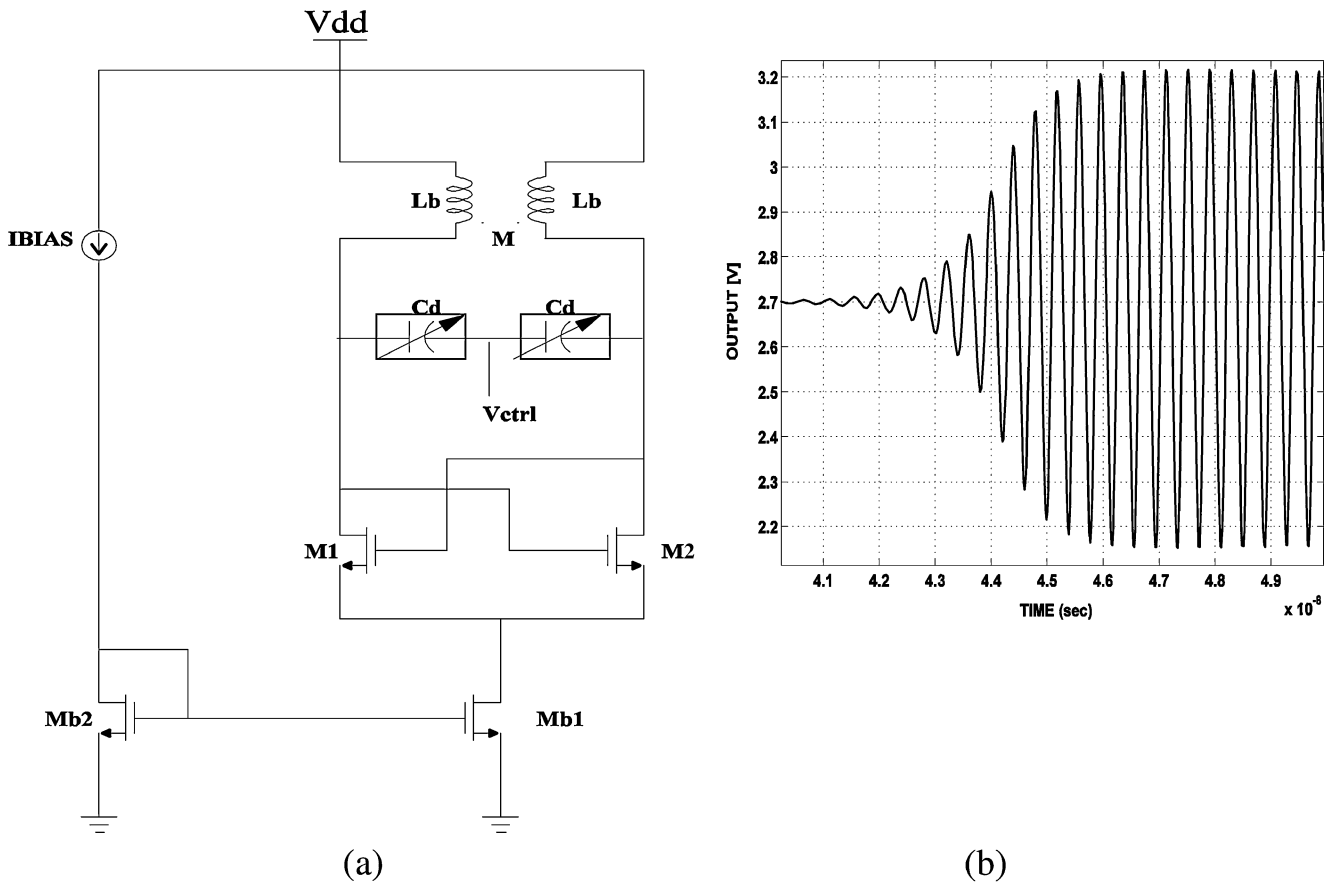


Fig. 8. (a) Schematic and (b) transient output of the VCO.

nickel/gold. The simulated results for the different MEMS capacitor structures have been summarized in Table I.

Simulations show that the polysilicon/gold structure offers the highest capacitance tuning ratio of 1.43:1. The aluminum structure offers a higher frequency tuning range of 19.2%. In addition, the three-parallel-plate capacitor offers an overall tuning ratio of 1.88:1 which is higher than the maximum theoretical value of 1.5:1 [12], [13]. However, the frequency tuning range

of 23.28% does not maintain the same trend due to the variable parasitic capacitance associated with this structure. The tuning characteristics of the different MEMS capacitor structures have been shown in Figs. 10 and 11. Cantilever beams show a linear tuning behavior owing to their low stiffness constants which, however, results in small deflections of the top plate at low *pull-in* voltages [22]. On the other hand fixed-fixed beams are highly nonlinear with higher stiffness constants for

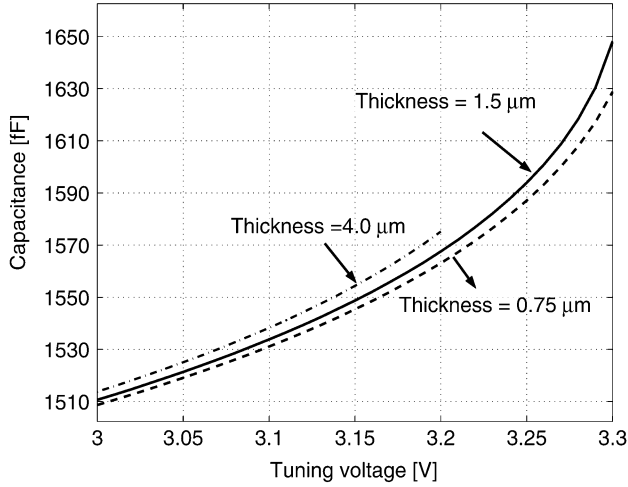


Fig. 9. Capacitance as a function of voltage for different thicknesses of the top plate.

TABLE I  
COMPARISON OF DIFFERENT MEMS CAPACITOR STRUCTURES

	Capacitance Tuning Ratio	Frequency Tuning Range
Cantilever Beam	1.18:1	6.4%
Fixed-Fixed Beam	1.27:1	0.6%
Polysilicon/Gold	1.43:1	14.6%
Aluminum	1.37:1	19.2%
Nickel/Gold	1.32:1	7.3%
Three-plate	1.88:1	23.28%

the same beam dimensions and therefore have high *pull-in* voltages [22]. However, the nonlinear behavior of fixed–fixed beams and the high tuning voltage requirements make them unsuitable for low voltage applications. Due to these factors the cantilever beam capacitor and the fixed–fixed beam capacitor show a poor tuning performance. Therefore, their characteristics have not been illustrated.

Experimental results for the 2.4-GHz VCO, employing the two-parallel-plate MEMS capacitor made up of polysilicon/gold have been presented in [15]. Table II provides a comparison between theoretical calculations [12], [15], our simulation results, and experimental data from [15].

Although the MEMS capacitor was designed for a nominal capacitance of 0.6 pF, a capacitance of 1.4 pF was measured. This is due to the top plate and bottom plate parasitic capacitances and high pad parasitic capacitances. As described in Section III, these parasitic capacitances have been accounted for in our simulations. Measured results also show a lower tuning range at a higher *pull-in* voltage. This discrepancy in the tuning range with measured results is due to residual stress [12], [22]. Since, the numerical analysis in EM8.9 does not account for residual stress, its effect is not seen in the simulated tuning characteristics.

## V. PHASE NOISE IN RF MEMS VCOS

Oscillator phase noise is a key parameter for high-performance communication systems. In a conventional *LC* oscillator, the electrical thermal noise and  $1/f$  noise contribute to the overall phase noise. However, in MEMS-based *LC*-tuned oscillators, an additional noise source due to the mechanical-thermal vibration is introduced. Vibrations of the suspended plate cause variations in the capacitance value and hence output phase noise.

### A. Brownian-Motion-Induced Phase Noise

In addition to classical phase noise, a MEMS-based *LC*-tuned oscillator introduces additional noise due to the mechanical-thermal vibration, also known as Brownian motion, from the variable capacitors. The displacement noise power spectral density can be computed as [21], [23]

$$\overline{X_n^2(\omega)} = \frac{4k_B T b}{k_m^2 \left[ \left(1 - \frac{\omega^2}{\omega_n^2}\right)^2 + \frac{1}{Q_M^2} \frac{\omega^2}{\omega_n^2} \right]} \quad (3)$$

where

- $\omega$  = frequency of interest;
- $k_B$  = Boltzman's constant;
- $T$  = temperature;
- $b$  = damping factor;
- $Q_M$  = quality factor of MEMS capacitor;
- $k_m$  = spring constant
- $\omega_n$  = mechanical resonant frequency.

For frequencies below and above  $\omega_n$ , (3) evaluates the displacement noise power spectral density to be  $4k_B T/mQ_M\omega_n^3$  and  $4k_B T\omega_n/mQ_M\omega^4$  respectively. At resonance the noise power spectral density can be computed to be  $4k_B TQ_M/m\omega_n^3$  [21]. Fig. 12 illustrates the displacement noise PSD for different values of  $Q_M$  for a typical MEMS capacitor design. The noise spectrum is seen to be white below  $\omega_n$  and falls with a slope of 40 dB per decade for frequencies higher than  $\omega_n$ . It can also be seen that the displacement noise decreases with an increase in  $Q_M$  for frequencies below and above  $\omega_n$ . However, peaks appear at the mechanical resonance frequency for  $Q_M$  greater than  $1/\sqrt{2}$ . In addition, the magnitude of these peaks increase with an increase in the value of  $Q_M$ .

Random thermal vibrations of the suspended plate cause variations in the capacitance value and hence result in mechanical thermal noise. The equivalent input current noise power spectral density can be computed by observing the current that arises from the change in capacitance due to Brownian motion. When a signal,  $v_{\text{sig}}$ , is applied across the MEMS capacitor, the displacement of the top plate is modulated around the DC bias displacement  $x_{\text{dc}}$  corresponding to an applied voltage  $v_{\text{sig(rms)}}$  [22]. The current noise that arises due to the change in the steady state capacitance can be expressed as a function of the displacement noise due to Brownian motion as given by (4)

$$\begin{aligned} i_{n,M} &= v_{\text{sig(rms)}} \cdot \frac{\partial C_D}{\partial t} \\ &= v_{\text{sig(rms)}} \cdot \left( \frac{\partial C_D}{\partial x} \right) \cdot \left( \frac{\partial x}{\partial t} \right)_{\text{noise}} \end{aligned} \quad (4)$$

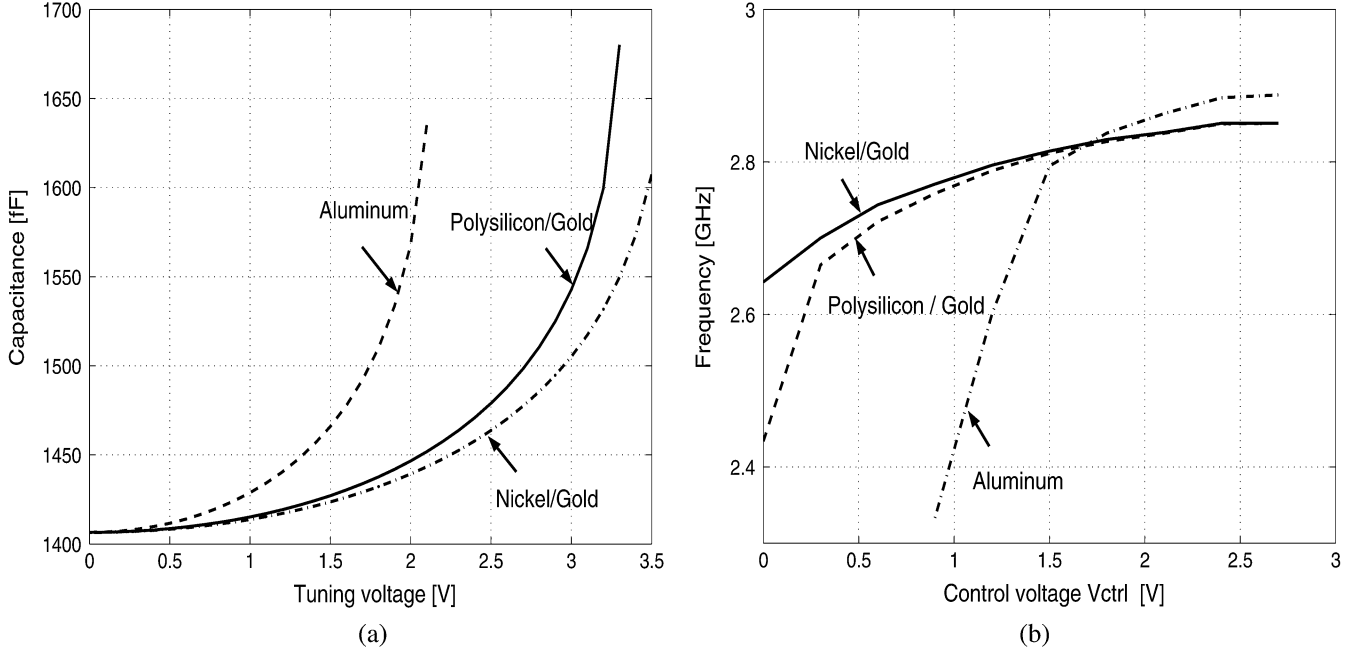


Fig. 10. (a) Capacitance as a function of voltage and (b) frequency as a function of voltage for the two-parallel-plate capacitor.

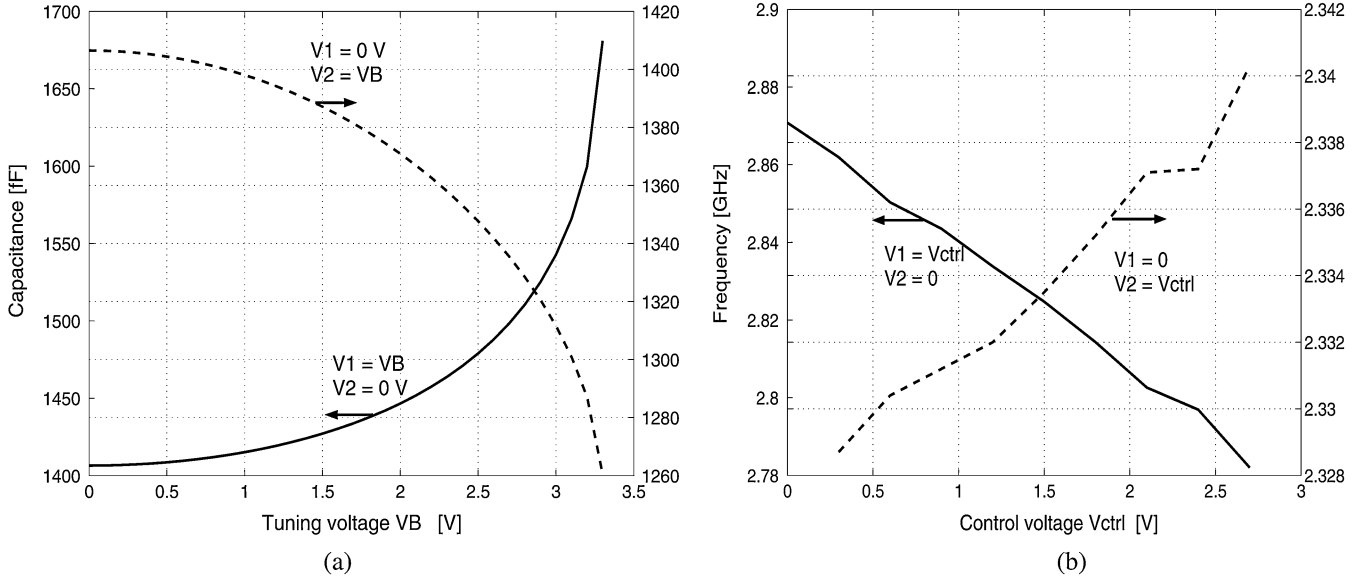


Fig. 11. (a) Capacitance as a function of voltage, and (b) frequency as a function of voltage for the three-parallel-plate capacitor.

For a signal frequency corresponding to the oscillation frequency  $\omega_0$ , (4) can be simplified to obtain the current noise power spectral density expressed as

$$\overline{i_{n,M}^2} = \frac{\omega_0^2 C_D^2 V_{\text{amplitude}}^2 \overline{X_n^2(\omega)}}{2(d+x)^2} \quad (5)$$

where  $V_{\text{amplitude}}$  is the amplitude of oscillation and  $\overline{X_n^2(\omega)}$  is the displacement noise power spectral density. An expression for the oscillator phase noise due to thermal noise, as given by (6), can be obtained by employing a transfer function approach based on a linear time-invariant (LTI) system analysis [21]. By using the expression for the input current noise power spectral density ((5)) and employing the transfer function approach, an expression for the phase noise due to Brownian motion can be

obtained and is given by (7). In the phase noise expressions provided below,  $P_{\text{rf}}$  is the oscillator RF output power,  $Q$  is the quality factor of the tank circuit and  $\eta$  is the ratio of the tank parasitic capacitance to the desired capacitance [21]

$$S_{\theta}(\Delta\omega)_E = \frac{kT}{2P_{\text{rf}}Q^2} \left( \frac{\omega_0}{\Delta\omega} \right)^2 \quad (6)$$

$$S_{\theta}(\Delta\omega)_M = \frac{\overline{X_n^2(\omega)}}{8(1+\eta)^2(d+x)^2} \left( \frac{\omega_0}{\Delta\omega} \right)^2. \quad (7)$$

From (6) and (7), the theoretical phase noise profiles due to electrical thermal noise,  $S_{\theta}(\Delta\omega)_E$ , and Brownian-motion,  $S_{\theta}(\Delta\omega)_M$ , are plotted in Fig. 13 for a typical design condition. The solid line shows the Brownian-motion-induced phase noise and the dashed line shows the phase noise due to

TABLE II  
COMPARISON OF SIMULATED RESULTS WITH THEORETICAL  
CALCULATIONS AND EXPERIMENTAL DATA

	Theoretical Calculations	Simulated Results* (this work)	Measured Results
Nominal Capacitance	0.6 pF	1.4 pF	1.4 pF
Capacitance tuning ratio	1.5:1	1.43:1	1.35:1
Pull-in Voltage	3.3 V	3.3 V	5.0 V
Frequency tuning range	18.35 %	14.6 %	3.4%

\*Simulated results include the effect of parasitics.

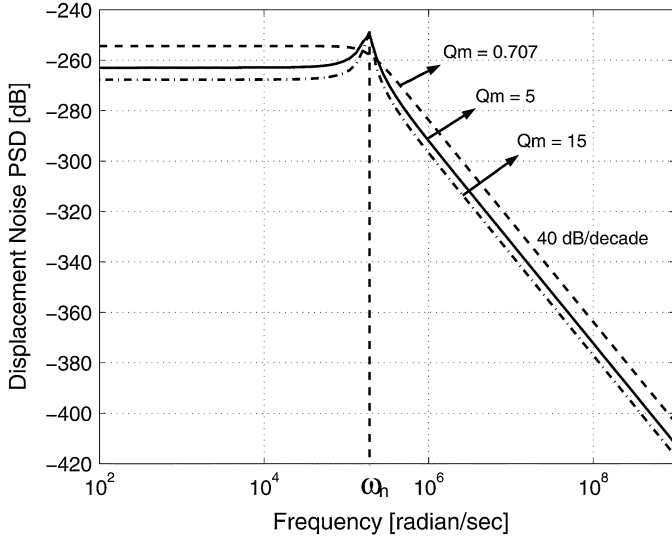


Fig. 12. Displacement noise power spectral density.

electrical-thermal noise. It is apparent that the Brownian-motion-induced phase noise is dominant for low offset frequencies. However, this noise decreases much faster than the classical phase noise above the mechanical resonant frequency,  $\omega_n = 30$  kHz, and eventually phase noise due to electrical thermal noise dominates. Peaking is observed in the phase noise profile at the mechanical resonant frequency. These peaks will increase as  $Q_M$  increases. Device  $1/f$  noise has not been taken into account here. In practice,  $1/f$  noise results in an increased noise level for low offset frequencies.

### B. Phase Noise Simulations

COSMO handles phase noise analysis based on a nonlinear perturbation analysis for oscillators [24]–[26]. The implemented technique allows for an accurate simulation of phase noise due to devices described either by analytical or numerical models.

Let  $x_s(t)$  be the steady-state solution of an unperturbed oscillator and let  $x_s(t + \alpha(t))$  be the steady-state solution of an oscillator with perturbation. The single-sided power spectral density,  $S_{ss}(f)$ , of  $x_s(t + \alpha(t))$  [25], [26] is given by

$$S_{ss}(f) = 2 \sum_{i=-\infty}^{\infty} X_i X_i^* \frac{f_0^2 i^2 c(f)}{\pi^2 f_0^4 i^4 c^2(f) + (f + i f_0)^2} \quad (8)$$

where

$f$  = frequency of interest and  $0 \leq f < \infty$ ;

$f_0$  = frequency of oscillation;

$i$  = the index of summation;

$X_i$  =  $i$ th Fourier series coefficient of  $x_s(t)$ ;

$c$  = a scalar that is a function of frequency.

The single-sideband phase-noise spectrum  $L(f_m)$  in dBc/Hz is given by

$$L(f_m) = 10 \log_{10} \left( \frac{S_{ss}(f_0 + f_m)}{2|X_1|^2} \right) \quad (9)$$

where  $f_m$  is the offset frequency from the carrier.

For  $0 \leq f_m \ll f_0$ , the single-sideband phase-noise spectrum  $L(f_m)$  in dBc/Hz can be approximated as [26]

$$L(f_m) = 10 \log_{10} \left( \frac{f_0^2 c(f_m)}{\pi^2 f_0^4 c^2(f_m) + f_m^2} \right) \quad (10)$$

where the scalar constant  $c(f_m)$  is frequency dependent. In the general case,  $c(f)$  is given by

$$c(f) = c_w \sum_{m=1}^M |c_{cm}(f_m)|^2 \quad (11)$$

where  $c_w$  is a contribution to the scalar  $c$  from white noise sources and is given by

$$c_w = \frac{1}{T} \int_0^T v_1^T(\tau) B_w(x_s(\tau)) B_w^T(x_s(\tau)) v_1(\tau) d\tau \quad (12)$$

and  $c_{cm}$  is the contribution to the scalar  $c$  from the  $m$ -th colored noise source and is given by

$$c_{cm} = \frac{1}{T} \int_0^T v_1^T(\tau) B_{cm}(x_s(\tau)) d\tau \quad (13)$$

where  $v_1(\tau)$  is the perturbation projection vector (PPV) [26]. The PPV is a periodic vector which serves as a transfer function from the noise sources to the scalar  $c$ , and hence to the overall phase noise power spectral density. The PPV scales the amount of noise transferred to the scalar  $c$  at each point of time.  $B_w$  is a state-dependent matrix that maps white noise sources with unity power spectral density (PSD) to the system of differential algebraic equations (DAEs) which describe a circuit.  $B_{cm}$  is a state-dependent vector that maps the  $m$ -th colored

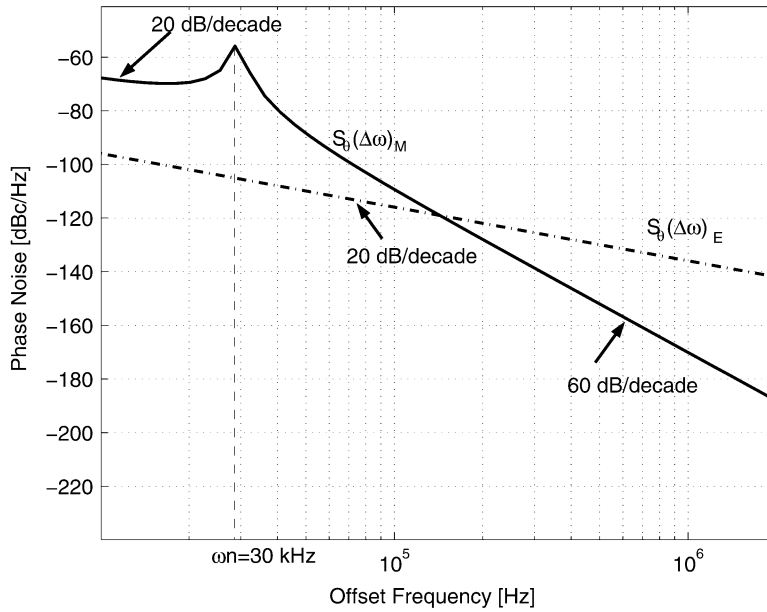


Fig. 13. Theoretical phase noise profiles of a MEMS VCO.

noise source to the system of DAEs. Thus, in order to obtain the single-sideband phase-noise spectrum  $L(f_m)$  in dBc/Hz, first a scalar  $c$  ((11)) needs to be calculated using (12) and (13) followed by computation of the phase-noise spectrum using (10). The method to obtain the PPV and matrices  $B_w$  and  $B_{cm}$  is described in [27].

The overall flowchart of the phase noise implementation is shown in Fig. 14, [27]. The first part of the algorithm was implemented in the transient analysis routine, where all the necessary data was collected and saved. The second part of the algorithm, which deals with the phase noise calculation itself, was implemented as a separate analysis (pnoise analysis). The sequence of operations is as follows. First, a transient analysis is run for a long enough time to ensure that the circuit reaches a steady state. During transient analysis, the period of oscillation  $T$  has to be calculated. When the period of oscillation is known, a time interval of one period has to be taken to save all the necessary data for phase noise calculation. At each time point of this time interval, the  $C$  (capacitance) and  $G$  (conductance) circuit matrices have to be saved, state-dependent noise sources have to be evaluated and the matrix  $B_w$  (for white noise sources) and the vectors  $B_{cm}$  (for colored noise sources) have to be stamped and saved.

In order to compute the additional phase noise due to the MEMS capacitor, the equivalent input noise needs to be evaluated. The values of the MEMS capacitor current noise sources are calculated using (3) and (5). The capacitance  $C_D$  and the displacement  $x$  are obtained from the device simulator EM8.9 [9] and the frequency of oscillation  $\omega_0$  and the amplitude of oscillation  $V_{amplitude}$  are obtained from a transient analysis.

The phase-noise calculation routine starts with the perturbation projection vector calculation (PPV) and then the scalar  $c$  is calculated. Finally, the single-sideband phase-noise spectrum  $L(f_m)$  in dBc/Hz is calculated using (10).

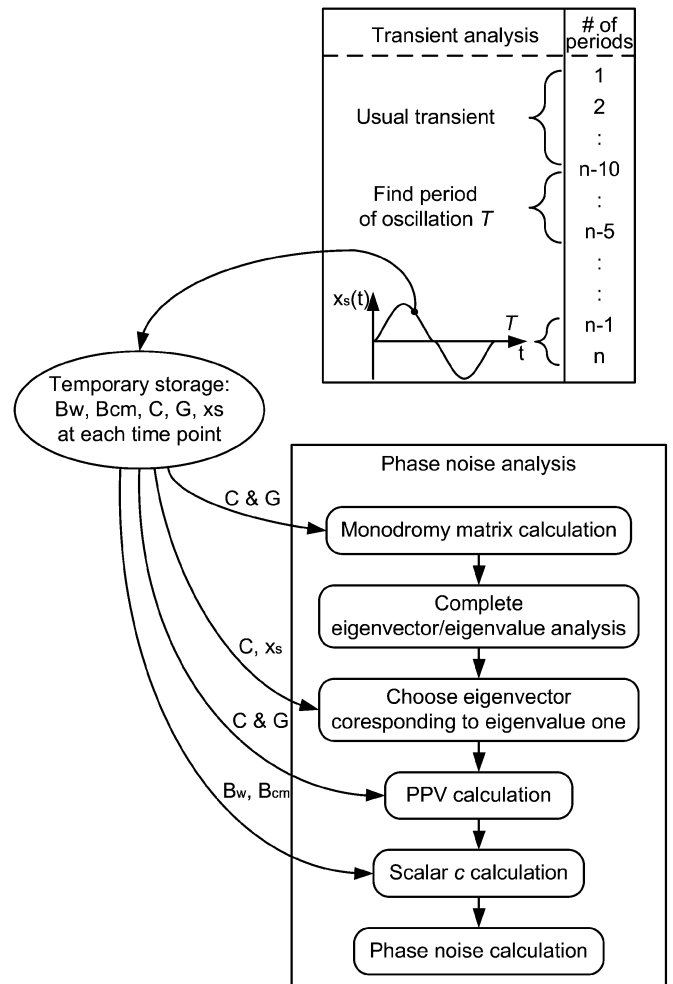


Fig. 14. A flowchart of the phase noise analysis implementation in COSMO.

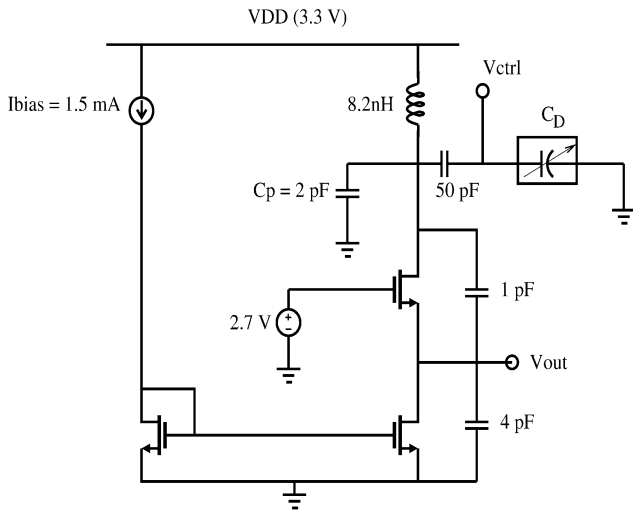


Fig. 15. VCO circuit for phase noise simulations.

## VI. PHASE NOISE SIMULATION RESULTS

An 800-MHz single-ended Colpitts VCO [14], [21] implemented in a HP 0.8  $\mu\text{m}$  CMOS technology was simulated to validate the phase noise simulations. The schematic of the VCO is as shown in Fig. 15. The 2.4-GHz VCO (Fig. 8) could not be simulated for phase noise due to unavailability of design parameters. A two-parallel-plate MEMS capacitor made up of aluminum [21] was employed and designed for an overlap area of 200  $\mu\text{m} \times 200 \mu\text{m}$  and an air-gap of 1.5  $\mu\text{m}$  to obtain a nominal capacitance of 0.2 pF. However, due to the top plate parasitic capacitance, a nominal capacitance of 0.5 pF is obtained. Four of these capacitors are connected in parallel for a total nominal capacitance of 2 pF. For a tuning voltage of 3 V, a maximum capacitance tuning ratio of 1.5:1 can be achieved by a suspension spring constant of 3.8 N/m [21]. The mass of the suspended top plate is taken as 100 ng corresponding to a mechanical resonant frequency of 30 kHz [21]. Based on this initial design, Table III provides a comparison between simulation and measurement results.

Equations (3) and (5) show that the noise in the MEMS capacitor is a function of the oscillation frequency  $\omega_0$  and the mechanical resonance frequency  $\omega_n$ . Therefore, in order to ensure valid comparisons between the simulated phase noise and that obtained from measurements, it is important that  $\omega_0$  and  $\omega_n$  be the same for both cases. Hence, the tank parasitic capacitance  $C_P$  was increased to obtain a simulated oscillation frequency of 721 MHz and a higher value for the mass of the MEMS capacitor was taken to obtain a simulated resonance frequency of 20 kHz.

From (5) it can be seen that the noise from the MEMS capacitor also depends on the capacitance of the MEMS capacitor. In order to validate the simulated phase noise, it is important to compare the simulated capacitance of the MEMS capacitor with experimental data. Fig. 16 shows the capacitance of the MEMS capacitor as a function of the tuning voltage as obtained from COSMO simulations and measurements [21]. It can be seen from Fig. 16 that the simulations agree with measurements to within 7%.

TABLE III  
COMPARISON BETWEEN SIMULATION RESULTS AND MEASUREMENT RESULTS BASED ON THE SAME INITIAL DESIGN ( $\omega_n = 30$  kHz,  $\omega_0 = 800$  MHz)

	Simulation	Measurements*
Mechanical resonant frequency ( $\omega_n$ )	29.3 kHz	20 kHz
Oscillation frequency ( $\omega_0$ )	787 MHz	721 MHz

\*Measured data from [21].

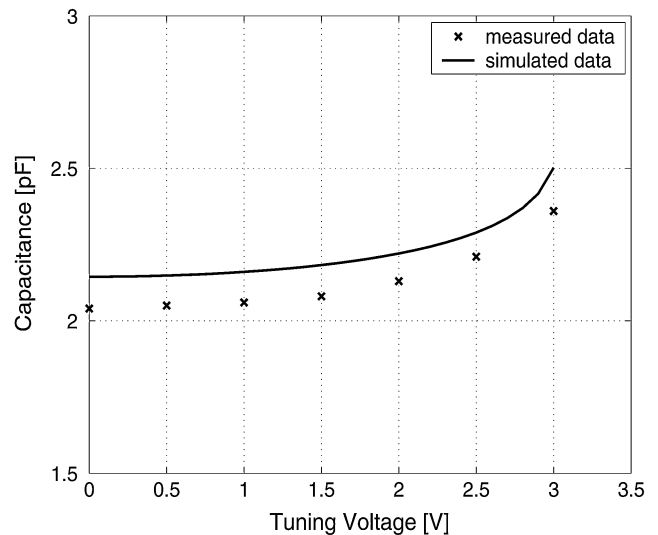


Fig. 16. Capacitance as a function of the tuning voltage of the MEMS capacitor used for phase noise simulations.

Fig. 17 shows the simulated phase noise spectrum of the modified MEMS VCO. The contribution of the individual noise sources is also illustrated. These trends are in agreement with the theoretical phase noise profile as discussed in Section III (see Fig. 13). Device  $1/f$  noise has been taken into account in these simulations. At low offset frequencies,  $1/f$  noise dominates, and therefore, the phase noise of the MEMS VCO shows a 30 dB per decade fall. For frequencies higher than the mechanical resonant frequency of 20 kHz, the electrical-thermal noise dominates and the phase noise shows a decay of 20 dB per decade. At an offset frequency equal to the mechanical resonant frequency, the phase noise is enhanced due to the peaking in the mechanical-thermal noise PSD at mechanical resonance.

Analysis of (3) and (5) shows that the only way to suppress the additional phase noise contributed by the MEMS capacitor is by increasing  $Q_M$  [21]. However, it has also been shown that at the mechanical resonance frequency the phase noise is enhanced due to the increased  $Q_M$ . The measured output power spectrum of the VCO under consideration (Fig. 15) reveals two main side-band peaks occurring at 20 kHz away from the carrier [21]. The simulated phase noise spectrum for different values of  $Q_M$  has been shown in Fig. 18. It can be seen that the peaks occur at the mechanical resonance frequency, i.e., at 20 kHz offset from the carrier. It can also be observed that the magnitude of these peaks increases with an increase in  $Q_M$ . Furthermore, from Fig. 18 it

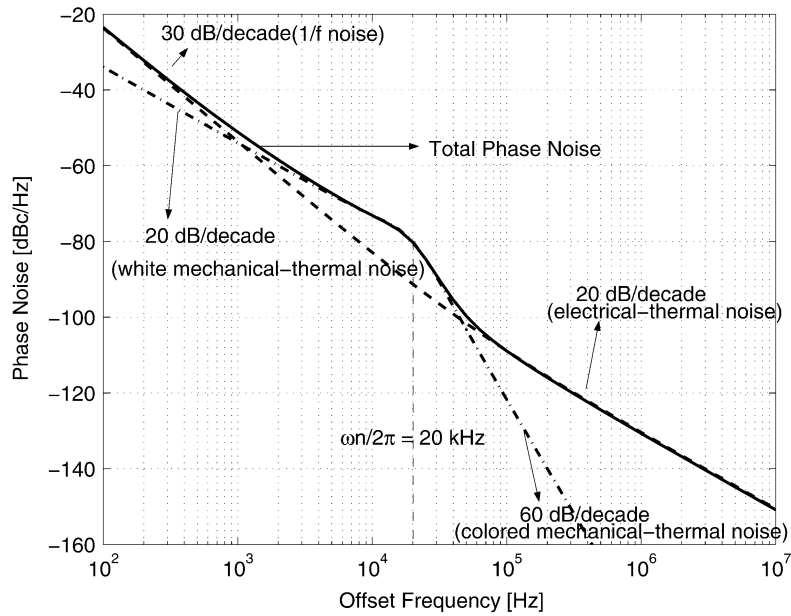


Fig. 17. Simulated phase noise spectrum ( $Q_M = 1$ ) of the MEMS VCO and contribution of the different noise sources.

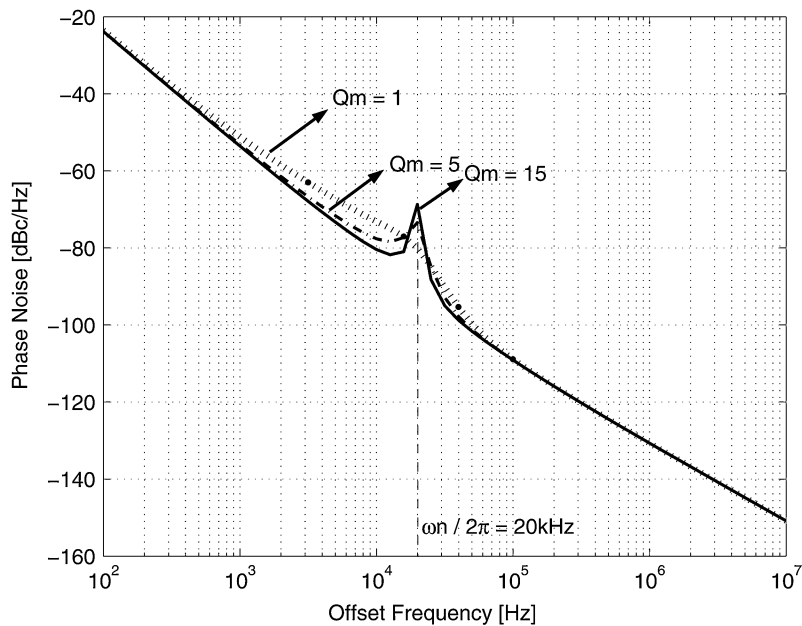


Fig. 18. Simulated phase noise spectrum ( $Q_M = 1, 5, 15$ ) of the MEMS VCO.

can be seen that a noise enhancement of 15 dB is obtained for  $Q_M = 15$  which is in agreement with experimental data [21].

Table IV provides the simulated values of the total phase noise for different values of  $Q_M$ . An improvement in phase noise can be seen for increasing  $Q_M$  for low offset frequencies. However, as the offset frequency gets higher, the dependence of phase noise on  $Q_M$  reduces. It can be seen from Table IV that there is good agreement between the simulated results and experimental data.

## VII. CONCLUSION

A new coupled circuit and device simulator, COSMO, has been presented for the design of low-phase noise RF MEMS

VCOs. The simulator was successfully used for a wide variety of MEMS capacitor structures, ranging from the simplest cantilever and fixed-fixed beam capacitors to the novel and recent three-parallel-plate, wide tuning range MEMS capacitor. The effect of different structural materials for the MEMS-based capacitors on the overall performance of the MEMS VCO has also been presented. A simulation method to accurately simulate the phase noise of RF MEMS VCOs has been described. Simulated results have been compared with experimentally observed behavior. The observed discrepancies can be attributed to combined effects of parasitic capacitances and residual stress. The simulator provides accurate results and can be used for the improved design of RF MEMS VCOs.

TABLE IV  
SUMMARY OF PHASE-NOISE SIMULATIONS AND COMPARISON  
WITH MEASURED DATA

Offset Frequency	Measured ( $Q_M = 15$ )	Simulated ( $Q_M = 15$ )	Simulated ( $Q_M = 5$ )	Simulated ( $Q_M = 1$ )
10 kHz	-81	-80.4	-77.6	-73.1
100 kHz	-110	-109.1	-109.1	-108.9
3 MHz	-139	-140.8	-140.8	-140.8

#### ACKNOWLEDGMENT

The authors thank T. Dudar for several useful discussions regarding this work.

#### REFERENCES

- [1] S. Senturia, "CAD challenges for microsensors, microactuators, and microsystems," *Proc. IEEE*, vol. 86, pp. 1611–1626, Aug. 1998.
- [2] T. Mukherjee, G. K. Fedder, D. Ramaswamy, and J. White, "Emerging simulation approaches for micromachined devices," *IEEE Trans. Computer-Aided Design Integr. Circuits Syst.*, vol. 19, pp. 1572–1588, Dec. 2000.
- [3] S. D. Senturia, R. M. Harris, B. P. Johnson, K. Songmin, K. Nabors, M. A. Shulman, and J. White, "A computer-aided design system for microelectromechanical systems (MEMCAD)," *J. Microelectromech. Syst.*, vol. 1, pp. 3–13, Mar. 1992.
- [4] K. Nabors and J. White, "FastCap: A multi-pole accelerated 3-D capacitance extraction program," *IEEE Trans. Computer-Aided Design Integr. Circuits Syst.*, vol. 10, pp. 1447–1459, Nov. 1991.
- [5] J. M. Funk, J. G. Korvinkj, J. Buhler, M. Bachtold, and H. Baltes, "SOLIDIS: A tool for microactuator simulation in 3-D," *J. Microelectromech. Syst.*, vol. 6, pp. 70–82, Mar. 1997.
- [6] S. Crary and Y. Zhang, "CAEMEMS: An integrated computer-aided engineering workbench for micro-electro-mechanical systems," in *Proc. IEEE Micro Electro Mechanical Systems*, Feb. 1990, pp. 113–114.
- [7] N. R. Aluru and J. White, "A multi-level Newton method for mixed-energy domain simulation of MEMS," *J. Microelectromech. Syst.*, vol. 8, pp. 299–308, Sep. 1999.
- [8] —, "An efficient numerical technique for electromechanical simulation of complicated micro-electro-mechanical-structures," *Sens. Actuators A, Phys.*, vol. 58, pp. 1–11, 1997.
- [9] G. Li and N. R. Aluru, "Efficient mixed-domain analysis of electrostatic MEMS," *IEEE Trans. Computer-Aided Design Integr. Circuits Syst.*, vol. 22, pp. 1228–1242, Sep. 2003.
- [10] S. K. De and N. R. Aluru, "Full-Lagrangian schemes for dynamic analysis of electrostatic MEMS," *J. Microelectromech. Syst.*, vol. 13, pp. 737–758, Oct. 2004.
- [11] G. Li and N. R. Aluru, "A Lagrangian approach for electrostatic analysis of deformable conductors," *J. Microelectromech. Syst.*, vol. 11, pp. 245–254, Jun. 2002.
- [12] A. Dec and K. Suyama, "Micromachined electromechanically tunable capacitors and their applications to RF ICs," *IEEE Trans. Microwave Theory Tech.*, vol. 46, pp. 2587–2595, Dec. 1998.
- [13] J. Zou, C. Liu, J. Schutt-Aine, J. Chen, and S. Kang, "Development of a wide tuning capacitor for wireless communications systems," in *Proc. IEDM'00 Tech. Digest*, Dec. 2000, pp. 403–406.
- [14] D. Young and B. E. Boser, "A micromachined-based RF low-noise voltage-controlled oscillator," in *Proc. CICC-97*, May 1997, pp. 431–434.
- [15] A. Dec and K. Suyama, "Microwave MEMS-based voltage-controlled oscillators," *IEEE Trans. Microwave Theory Tech.*, vol. 48, pp. 1943–1949, Nov. 2000.
- [16] T. L. Quarles, "The SPICE3 Implementation Guide," Electronics Research Laboratory, University of California, Berkeley, CA, Memo no. UCB/ERL M89/44, Nov. 1989.
- [17] J. M. Huang, K. M. Liew, C. H. Wong, S. Rajendran, M. J. Tan, and A. Q. Liu, "Mechanical design and optimization of capacitive micromachined switch," *Sens. Actuators A, Phys.*, vol. 93, pp. 273–285, 2001.
- [18] F. D. Bannon, III, J. R. Clark, and C. T.-C. Nguyen, "High frequency microelectromechanical IF filters," in *Proc. IEDM'96 Tech. Digest*, Dec. 1996, pp. 773–776.
- [19] A. C. Wong, H. Ding, and C. T.-C. Nguyen, "Micromechanical mixers-filters," in *Proc. IEDM'98 Tech. Digest*, Dec. 1998, pp. 471–474.
- [20] J. R. Clark, F. D. Bannon, III, A.-C. Wong, and C. T.-C. Nguyen, "Parallel-resonator HF micromechanical bandpass filters," in *Proc. Transducers'97*, vol. 2, June 1997, pp. 1161–1164.
- [21] D. J. Young, "Micromechanical Devices and Fabrication Technologies for Radio-Frequency Analog Signal Processing," Ph.D. dissertation, Univ. of California, Berkeley, CA, 1999.
- [22] G. M. Rebeiz, *RF MEMS Theory, Design, and Technology*. New York: Wiley, 2003.
- [23] T. B. Gabrielson, "Mechanical-thermal noise in micromachined acoustic and vibration sensors," *IEEE Trans. Electron Devices*, vol. 40, pp. 903–909, May 1993.
- [24] A. Demir, A. Mehrotra, and J. Roychowdhury, "Phase noise in oscillators: A unifying theory and numerical methods for characterization," *IEEE Trans. Circuit Syst.-I*, vol. 47, pp. 655–674, May 2000.
- [25] A. Demir, "Phase noise in oscillators: DAE's and colored noise sources," in *Proc. IEEE/ACM Int. Conf. CAD*, Nov. 1998, pp. 170–177.
- [26] —, "Floquet theory and nonlinear perturbation analysis for oscillators with differential-algebraic equations," *International Journal of Circuit Theory and Applications*, pp. 163–185, Mar.–Apr. 2000.
- [27] V. Kratyuk, "Algorithms and Tools for Optimization of Integrated RF VCOs," M.S. thesis, Oregon State University, Corvallis, Jun. 2003.



**Manas Behera** received the Bachelor of Engineering degree in electronics and telecommunication engineering from University College of Engineering, Sambalpur, India, in 2001. He received the M.S. degree in electrical engineering from Oregon State University, Corvallis, in 2004.

He is currently with Epoch Microelectronics, Inc., Hawthorne, NY, as a Design Engineer. His current research interests include analog/RF design, analog circuit simulation and RF MEMS device modeling.



**Volodymyr Kratyuk** received the B.S. and the M.S. degrees (Hons.) in physical electronics from National Technical University of Ukraine "KPI", Kyiv, Ukraine, in 1997 and 1999, respectively, and the M.S. degree in electrical engineering from Oregon State University, Corvallis, in 2003. He is currently working toward the Ph.D. degree in electrical engineering at Oregon State University.

His current research interests include low-noise analog circuit design and frequency synthesizer design.



**Sudipto K. De** received the B.Tech. degree in mechanical engineering from the Indian Institute of Technology, Kharagpur, India, in 2000 and the M.S. degree from the University of Illinois at Urbana-Champaign in 2002. He is currently working toward the Ph.D. degree in mechanical engineering at the University of Illinois at Urbana-Champaign under Prof. N. R. Aluru.

His research interests include computational analysis and design of MEMS/Bio-MEMS and numerical methods in engineering.

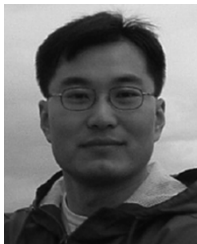


**Narayan R. Aluru** (M'00) received the B.E. degree with honors and distinction from the Birla Institute of Technology and Science (BITS), Pilani, India, in 1989, the M.S. degree from Rensselaer Polytechnic Institute, Troy, NY, in 1991, and the Ph.D. degree from Stanford University, Stanford, CA, in 1995.

He is currently an Associate Professor in the Department of Mechanical and Industrial Engineering at the University of Illinois at Urbana-Champaign (UIUC). He is also affiliated with the Beckman Institute for Advanced Science and Technology, the

Department of Electrical and Computer Engineering and the Bioengineering Department at UIUC. He was a Postdoctoral Associate at the Massachusetts Institute of Technology (MIT), Cambridge, from 1995 to 1997. In 1998, he joined the University of Illinois at Urbana-Champaign (UIUC) as an Assistant Professor.

Dr. Aluru received the NSF CAREER award and the NCSA faculty fellowship in 1999, the 2001 CMES Distinguished Young Author Award, the 2001 Xerox Award for Faculty Research, and the Willett Faculty Scholar Award in 2002. He is a Subject Editor for the IEEE/ASME JOURNAL OF MICROELECTROMECHANICAL SYSTEMS, Associate Editor for the IEEE TRANSACTIONS ON CIRCUITS AND SYSTEMS II and serves on the Editorial Board of a number of other journals.



**Yutao Hu** received the B.S. degree in electrical engineering from Tsinghua University, Beijing, China, in 1994, the M.S. degree in electrical engineering from Washington State University, Pullman, WA, in 1998, and the Ph.D. degree in electrical engineering from Oregon State University, Corvallis, in 2004.

He is now with Agilent Technologies, Santa Rosa, CA. His research interests are in the areas of circuit simulation, device simulation, and behavioral modeling.



**Kartikeya Mayaram** (S'82–M'88–SM'99–F'05) received the B.E. (Hons.) degree in electrical engineering from the Birla Institute of Technology and Science, Pilani, India, in 1981, the M.S. degree in electrical engineering from the State University of New York, Stony Brook, in 1982, and the Ph.D. degree in electrical engineering from the University of California, Berkeley, in 1988.

From 1988 to 1992, he was a Member of Technical Staff in the Semiconductor Process and Design Center of Texas Instruments, Dallas. From 1992 to

1996, he was a Member of Technical Staff at Bell Labs, Allentown. He was an Associate Professor in the School of EECS at Washington State University, Pullman, from 1996 to 1999 and in the Electrical and Computer Engineering (ECE) Department at Oregon State University, Corvallis, from 2000 to 2003. Currently, he is a Professor in the School of Electrical Engineering and Computer Science (EECS) at Oregon State University. His research interests are in the areas of circuit simulation, device simulation and modeling, integrated simulation environments for microsystems, and analog/RF design.

Dr. Mayaram received the National Science Foundation (NSF) CAREER Award in 1997. He was an Associate Editor of IEEE TRANSACTIONS ON COMPUTER-AIDED DESIGN OF INTEGRATED CIRCUITS AND SYSTEMS from 1995 to 2001 and has been the Editor-in-Chief of this journal since January 2002.